GEOPHYSICAL RESEARCH LETTERS, VOL. 35, L03304, doi:10.1029/2007GL032465, 2008

Sharpness of the D″ discontinuity beneath the Cocos Plate: Implications for the perovskite to post-perovskite phase transition

T. Lay[1]

Received 26 October 2007; revised 28 December 2007; accepted 3 January 2008; published 2 February 2008.

[1] The depth extent, or sharpness, of the D″ seismic velocity discontinuity is determined by modeling distance-dependence of reflected *S*-wave signals sampling the lowermost mantle beneath the Cocos Plate. The data, spanning distances from 64° to 83° and grouped in two small turning-point bins from 5° to 10°N and 10° to 15°N, are compatible with a sharp 1 to 2% shear velocity increase near 300 km above the core-mantle boundary, but not with reflection from a transition zone extending more than ~30 km in depth. Interpretation of the velocity structure as the result of magnesium-silicate perovskite undergoing a phase transition to post-perovskite requires limited presence of Al and Fe, which will broaden the phase transition. Current experiments indicate that the phase transition may occur over ~5 GPa (90 km) in pyrolitic material, requiring either distinct chemistry or dynamical mechanisms to sharpen the phase transition for this high-velocity sub-circum-Pacific region. **Citation:** Lay, T. (2008), Sharpness of the D″ discontinuity beneath the Cocos Plate: Implications for the perovskite to post-perovskite phase transition, *Geophys. Res. Lett.*, *35*, L03304, doi:10.1029/2007GL032465.

1. Introduction

[2] Phase transitions in abundant mantle minerals, such as olivine, are responsible for the principal abrupt increases in seismic velocities and density in the transition zone. Thus, it is quite natural to seek similar explanations for any lower mantle velocity discontinuities, including the rapid ~2.5% increase in *S*-wave velocity that occurs several hundred kilometers above the core-mantle boundary (CMB) in many locations [*Lay and Helmberger*, 1983; *Wysession et al.*, 1998]. The latter structure, often called the D″ discontinuity due to its location at the top of the D″ region in the lowermost mantle, has been enigmatic for decades, but a recently discovered phase transition of the most abundant lower mantle mineral $(Mg_{1-x},Fe_x)SiO_3$ magnesium-silicate perovskite (Pv) to post-perovskite (PPv) may provide an explanation [*Murakami et al.*, 2004]. This phase transition predicts a several percent increase in *S*-wave velocity with little change in *P*-wave velocity for pressure-temperature (P-T) conditions expected for the lowermost mantle.

[3] If the Pv-to-PPv transition is responsible for the seismically observed D″ discontinuity, experimental and theoretical calibration of the phase boundary P-T properties provides a valuable thermometer and compositional probe for the lowermost mantle. Reconciling the seismic observations with predicted behavior for the phase transition is viable as long as strong thermal and chemical heterogeneities are present in D″ [*Lay and Garnero*, 2007], but improved constraints from both seismology and mineral physics are needed. One open issue is the pressure range over which the phase transition occurs, which is manifested in the depth extent, or sharpness of the D″ discontinuity. We address this issue with a high quality seismological data set and assess the implications for the phase transition hypothesis.

2. Data and Methods

[4] Determining the sharpness of seismic velocity changes in the mantle is difficult, with the best constraints for upper mantle discontinuities being obtained by underside reflections of high frequency signals at near vertical angles of incidence. For the D″ discontinuity, the velocity and impedance contrasts are small, and there are few, if any, reliable observations of near-vertical reflections. Significant reflection amplitudes are only observed at large distances, where wide-angle reflections from a velocity increase are enhanced by critical angle phenomena. Consequently, almost all reliable observations of reflections from the D″ discontinuity are at ranges greater than 65°, where *S* wave triplications are observed [*Lay and Helmberger*, 1983]. Wide-angle reflections are primarily sensitive to velocity contrasts, but grazing raypaths at post-critical distances have very limited sensitivity to sharpness of the velocity jump. However, for relatively short-period waves there is some sensitivity to sharpness for signals straddling the pre-critical to post-critical range, though one needs to have data sampling a localized reflector position with variable angles of incidence. Short-period *S*-wave signals for multiple events and stations sampling a localized D″ region with raypaths spanning a wide-angle range of epicentral distances of several tens of degrees would allow the sharpness of the D″ discontinuity to be constrained fairly well. A data set satisfying these demanding conditions exists for paths traversing the lowermost mantle beneath the Cocos Plate.

[5] The same *SH*-wave data set analyzed by *Lay et al.* [2004], *Thomas et al.* [2004], and *Hutko et al.* [2006], comprised of recordings of deep South American earthquakes from broadband stations in California, is used here. These data densely sample the lowermost mantle beneath the Cocos Plate (Figure 1); waveforms and source details are presented in the earlier papers. The earlier studies used stacking and migration approaches, finding clear *S*-wave triplication arrivals accounted for by a several percent increase in shear velocity near 250 to 350 km above the CMB. The velocity increase was assumed to be sharp in the modeling. Lateral variations in the velocity structure and

[1]Department of Earth and Planetary Sciences, University of California, Santa Cruz, California, USA.

0094-8276/08/2007GL032465$05.00

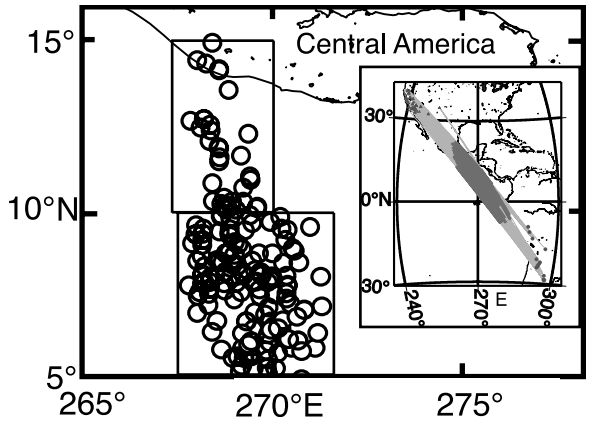

Figure 1. Map showing *ScS* CMB reflection points (circles) for *SH*-waves from intermediate depth and deep South American earthquake recorded at broadband stations in California. The data are grouped in two bins from 5° to 10°N and 10° to 15°N. The map position of the *ScS* raypaths, with the portion of the paths in the lowermost 300 km of the mantle highlighted (dark gray), are shown in the inset.

discontinuity depth are both present, but relatively stable behavior of the data was found for signals with *ScS* CMB reflection points north of 5°N. The dominant periods of the data after processing to equalize and enhance the bandwidth by source wavelet deconvolution are 3–4 s, which is about the shortest period recoverable for teleseismic *S* signals. With little, if any, *P*-wave reflectivity from D″ in this region, these are the shortest wavelength (~20–30 km) signals available to examine the sharpness of the local *S*-wave velocity increase.

[6] The data are grouped into two subsets (Figure 1), involving *ScS* reflection points from the CMB in bins from 5° to 10°N (138 signals with epicentral ranges from 71° to 83°) and 10° to 15°N (58 waveforms with epicentral ranges from 64° to 83°). Ideally, the data would have identical turning points, but this is not practical due to data sampling limitations and the need for stacking many traces to suppress noise in the individual seismograms. The bin dimensions of about 250 km at the CMB are about the effective Fresnel zone of our data, and must entail some lateral averaging of structure, but it is possible to assess whether internal variations across the bins are significant, as noted below.

[7] The basic *S*-wave velocity structure for each subregion is characterized by performing double-array stacking of all data sampling each bin and modeling the resulting stacks by identical processing of reflectivity synthetics computed for a localized 1D model [*Lay et al.*, 2004]. In the stacking procedure a reference phase is chosen for phase alignment and amplitude normalization; for each bin we separately use *S* and *ScS* as reference phases, obtaining two

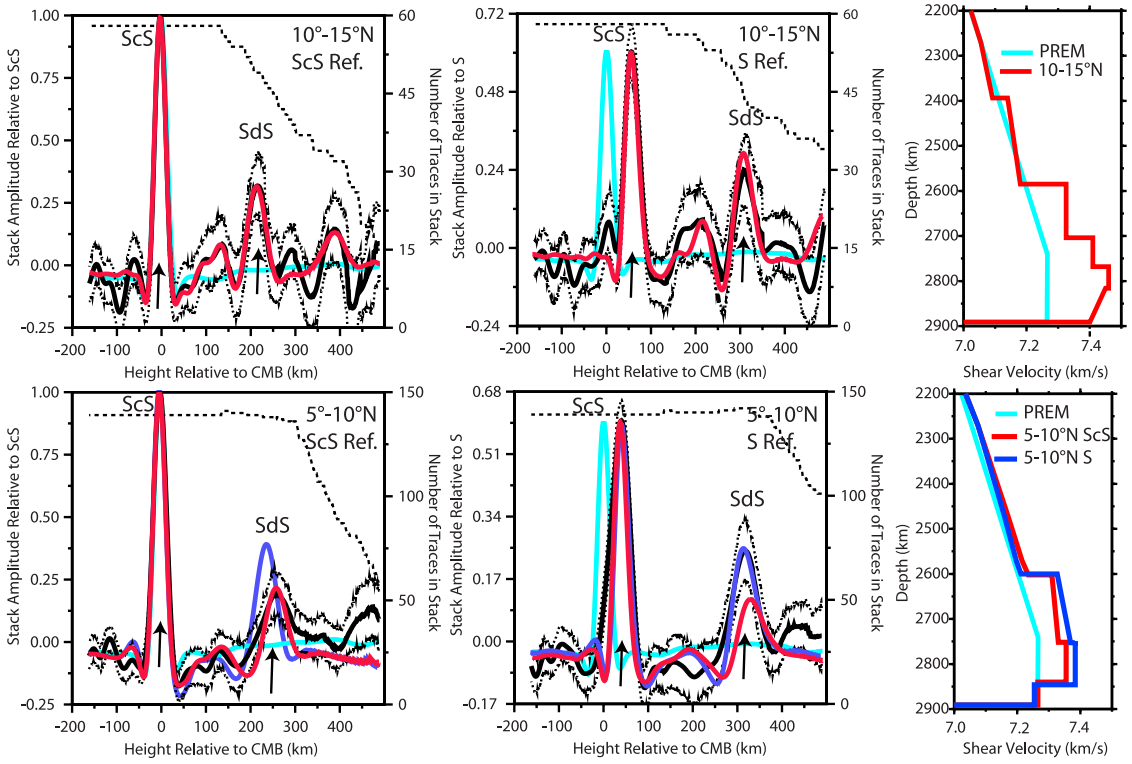

Figure 2. Double array stacks for the data sampling each of the bins in Figure 1: (left) alignment on *ScS* as a reference phase and (middle) alignment on *S* as a reference phase. The amplitude of the data stack at various target depths relative to the CMB is shown (bold black lines; left scales), along with bootstrap-estimated variance of the stack (dotted black lines). Arrows indicate the *ScS* and *SdS* features. Short dashed lines indicate the number of traces contributing to the stack at each target depth (right scales). Red, blue and cyan lines correspond to stacking of synthetics for the (right) corresponding velocity models, fit by trial and error to the data, along with model PREM, which has no *SdS* reflection.

different stacks. The corresponding data stacks are shown in Figure 2. When modeling the stacks that have *ScS* as a reference, we go beyond the procedure of *Lay et al.* [2004], to ensure that the final velocity model also matches the depth alignment of *ScS* arrivals when *S* is used as a reference phase. This explicitly matches the *ScS-S* differential times, ensuring a suitable background velocity structure. We also model more subtle features in the stacks than in previous work, allowing for complexity within the D″ layer below the shallowest velocity increase. PREM is used as a reference migration structure for all data and synthetic stacks.

[8] The resulting velocity structures and model fits are also shown in Figure 2. The velocity structures all have a prominent shear velocity discontinuity near 2600 km depth, along with smaller velocity increases within the D″ layer and minor velocity reductions above the CMB. There is about a 10 km uncertainty in the depth of the sharp D″ reflector; a level of precision achieved by matching the *ScS-S* differential times along with all significant features in the stacks. The slight (~20 km) difference in the discontinuity depth between the bins and the differences in average velocity levels in the lowermost 400 km of the mantle are required by the data, and compatible with prior migrations and tomography results. The velocity decreases at the base of the mantle may possibly be related to back-transformation of PPv to Pv [see *Hernlund et al.*, 2005], but here we focus on sharpness of the velocity increase near 2600 km depth.

[9] For the 5° to 10° bin, we obtain two models, one matching the stack aligned on *ScS* (red) and one matching the stack aligned on *S* (blue). The strength of the reflector near 2610 km depth, which produces the *S* wave reflection/triplication arrival labeled *SdS*, varies by almost a factor of two between the models for this bin, because the choice of reference phase affects the coherence of the *SdS* and/or *ScS* phases. This presumably results from lateral variations in structure affecting the waveforms sampling the small bin. We use the stacks for both reference phases to assess sharpness of the reflector for this region, but recognize that lateral heterogeneity likely competes with sharpness in controlling the *SdS*/*ScS* amplitude ratios in this bin. For the 10° to 15° bin the preferred velocity model's fit to the stack aligned on *ScS* also fits the stack aligned on *S* well, so there appears to be minimal effects of lateral variations across the northern bin. The sharpness estimates obtained below by modeling the data for this bin are thus deemed the most reliable.

3. Sharpness of the Velocity Increase

[10] Synthetic seismograms are computed for perturbations of the basic models in which the same overall velocity increase centered near 2600 km is retained, but the increase is distributed linearly over transition zones with widths ranging from 0 to 100 km. Phase transitions likely go to completion with a non-linear rather than a linear increase in the high pressure component with depth, but the available seismic data do not have sufficient resolution to warrant a more complex parameterization than a linear gradient. As the transition zone thickens, closer in (pre-critical) reflections weaken, while the wide-angle (post-critical) triplications change only slowly. The fit to the data is not optimized for each transition zone model, which would require small depth and velocity increase adjustments, but instead the focus is on the behavior of the *SdS* reflected energy as a function of transition zone width. Stacks of synthetics spanning the full distance range of the data for each bin, like those in Figure 2, are very slowly varying since they tend to be dominated by the larger amplitude post-critical arrivals at the largest distances. However, by subdividing the data for a given bin into several distance bands for which there is still sufficient sampling to get a meaningful stack, observable *SdS*/*ScS* amplitude variations can be compared to similarly windowed subsets of synthetics.

[11] Figure 3 shows the distance-dependence of *SdS*/*ScS* amplitudes for stacked data and synthetics with either *ScS* or *S* being the reference phase for the stacks in each bin. The distance range spanned by each substack is indicated along with the bootstrap resampling estimated standard error of the mean observed stacked *SdS*/*ScS* amplitude ratio. Corresponding calculations for a sharp D″ discontinuity, and for increases distributed over 30-, 60- and 90-km are shown. The data coverage and numbers suffice to compute 3 distance-range substacks for each bin. An acceptable model should fit both the absolute levels and the trends with distance. As expected, the sharp models fit the two larger distance observed ratios very well for each data bin, as do models with discontinuities distributed over up to 30 km. Broader transitions of up to 60 km thickness can still match the data at the largest distances, but they under-predict the middle and closest distance ranges. Yet broader transitions produce weaker arrivals at all distances and predict even stronger distance trends, at odds with the data (even if one increases the magnitude of the velocity increase to match the most post-critical observations, the models still significantly under-predict the closer data).

[12] The data for the 5° to 10° bin have anomalously low *SdS*/*ScS* amplitudes at the closest distances, and all of the models that fit larger distances fail to match this. This appears to represent defocusing of the closer *SdS* arrivals due to the lateral heterogeneity noted above, rather than sharpness of the reflector, as it occurs for the stacks relative to both *ScS* and *S*. The observations in the two larger distance bins are intrinsically more reliable due to larger *SdS* amplitudes and are most consistent with a sharp discontinuity, or a transition zone up to 30 km in extent. For the more stable 10° to 15°N bin, the data at the smallest distance, although well pre-critical, do have an impulsive coherent stacked *SdS* feature (Figure 4). The sharp discontinuity matches this amplitude within the uncertainty, and the 30-km transition zone is almost acceptable, while thicker transitions under-predict the amplitude by factors of up to 3 to 4, strongly favoring the sharper structures.

[13] In addition to the amplitude variations with distance, the shape of the *SdS* stacks varies with transition zone thickness, and this provides additional constraints on what models are acceptable. The double-array stacks aligned on *ScS* for the three distance subsets for the 10° to 15° bin are shown in Figure 4a. Clear *SdS* features are observed at all ranges, with decreasing amplitude and slightly decreasing apparent depth for closer distances. The latter effect is a predictable consequence of stacking of triplication arrivals, which actually turn at greater depths as distance increases;

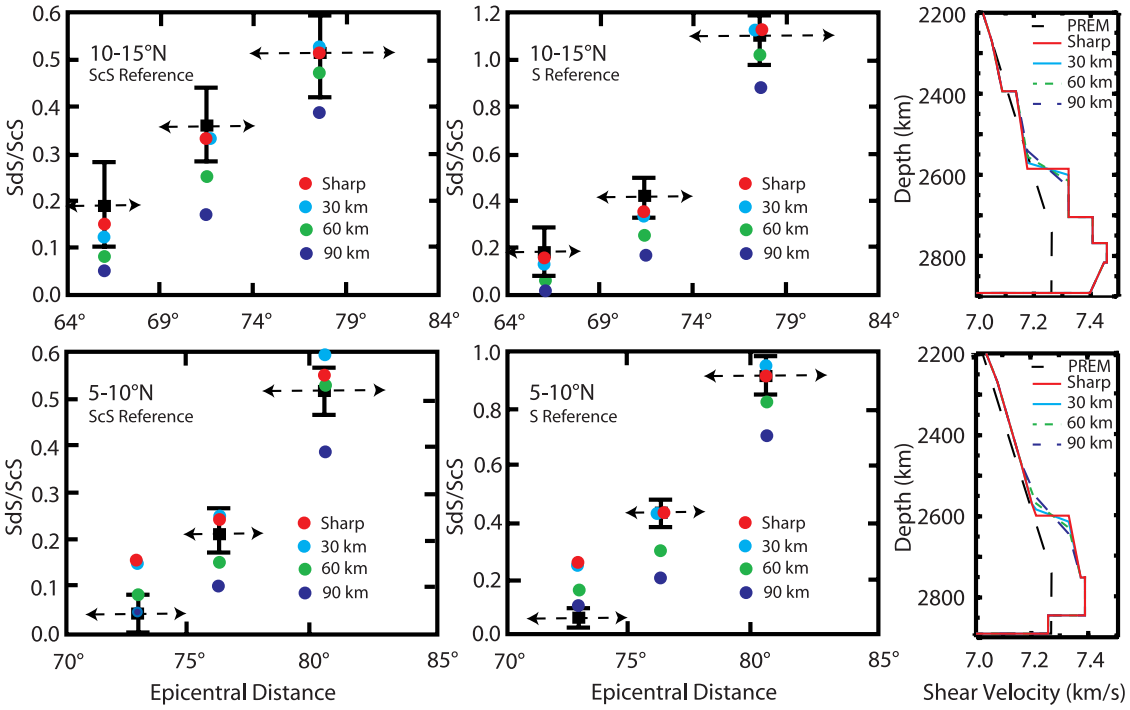

Figure 3. *SdS*/*ScS* amplitude ratios for data (black boxes with error bar corresponding to standard error of the mean ratio) for stacks of subsets of data relative to (left) *ScS* or (middle) *S* in different distance ranges (indicated by the dashed double-headed arrows) and for synthetics for the (right) color-coded velocity models. Data and models for the 10 to 15° bin are shown at the top, while the 5° to 10° data and models (based on the stacks on *S*) are shown below.

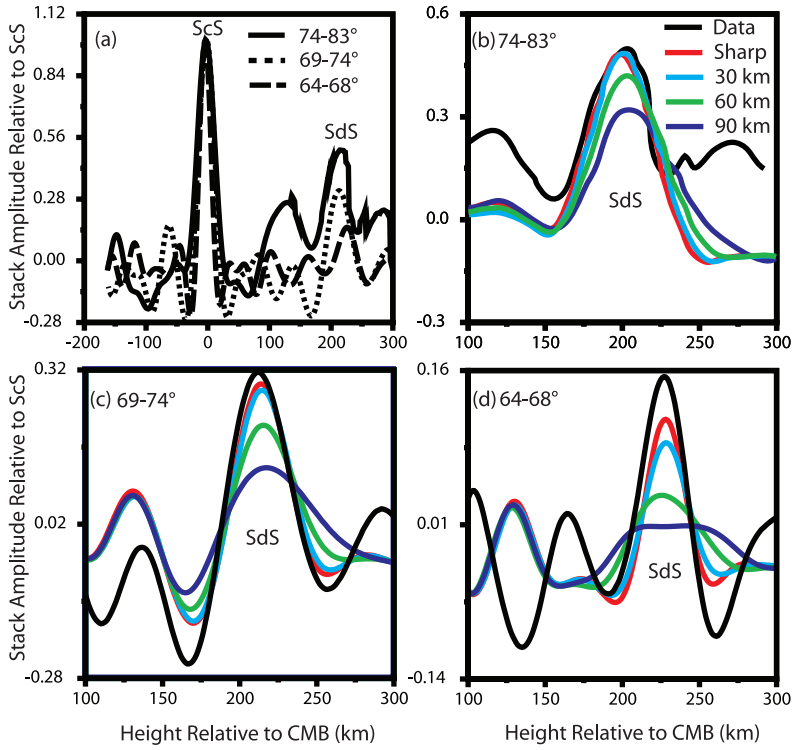

Figure 4. Double array stacks of subsets of data in the 10° to 15° bin (a) for the entire D″ depth range and zoomed in on the *SdS* feature for data in the distance ranges (b) 74° to 83°, (c) 69° to 74°, and (d) 64° to 68°. Figures 4b–4d include the stacks showing *SdS* for the gradient models with the same color-coding from Figure 3 (top).

double-array stacking forms the strongest image of the triplicated signal at the best apparent reflector depth assuming only pre-critical reflections. Figures 4b–4d compare the data and synthetic stacks for the models shown in the upper right of Figure 3. At the largest distances (Figure 4b), the stacked synthetics for transition zones up to 60 km wide match the data, but the 60-km transition zone models are too broad and too low in amplitude to match the data at 64 to 68° (Figure 4d). Similar general trends are found for the other bin and for the stacks using alternate reference phases. Similarity of the pulse width of *ScS* and *SdS* features ensures that there are no affects of anomalous attenuation.

[14] Overall, the data are consistent with velocity increases in both bins that are either sharp or distributed over no more than ~30 km in depth. The 5° to 10°N bin appears to have internal variations that can defocus the *SdS* and *ScS* arrivals, but even with this, the larger distance arrivals favor a sharp discontinuity. Larger transition zone depth ranges produce too strong of a predicted amplitude variation with distance and too broad of a stacked image for the pre-critical data. Improved constraints should be obtainable by using larger data sets and data spanning more distance range, but for the specific region under the Cocos Plate considered here, the earthquake source distribution and broadband station locations do not allow improved distance sampling, so adding new data as they become available is the only option for this region. The evidence for lateral variation in structure over an only 250 km wide turning-point bin, as in the 5° to 10°N bin, motivates consideration of very localized spatial samples having turning rays from many distances. In practice, this is challenging to achieve, but confidence will not be high for large spatial gathers.

4. Discussion

[15] A univariant Pv-PPv transition in pure $MgSiO_3$ is expected to be quite sharp, slightly broadened by any temperature gradient, and most experiments and theory have been conducted for this end-member composition perovskite. However, Fe and Al can substitute in magnesium perovskite, and this will tend to distribute the transition over a broader pressure range. For example, in the presence of only 6.25 mol% Al_2O_3, the transition is calculated to extend over 150 km (127–140 GPa) [*Akber-Knutson et al.*, 2005]. The presence of Fe can also produce an extensive two-phase domain [*Mao et al.*, 2004; *Tsuchiya and Tsuchiya*, 2006; *Tateno et al.*, 2007], although there are still uncertainties in the specific effects of iron on the phase transition [*Hirose*, 2006]. Experiments on MORB and pyrolitic compositions, which are even more complex, indicate a two-phase regime extending about 5 GPa (~70 km depth range in D″) for these materials [*Ohta et al.*, 2008]. This significantly exceeds the 30 km (<2 GPa) upper bound estimated in this paper, as well as a comparable bound for the structure under Alaska estimated from a small number of waveforms. While further seismological analysis is desirable, the current constraints from mineral physics and seismology suggest that if the D″ discontinuity under the Cocos Plate is caused by the Pv-PPv phase transition, there is relatively little Al and Fe present in the perovskite composition. Partitioning of Fe into (Mg,Fe)O accompanying spin-transition, yielding low-Fe perovskite, may be one mechanism operating in the lowermost mantle.

[16] **Acknowledgments.** BDSN, Trinet and IRIS data centers provided data. Supported by NSF grant EAR0635570. I thank V. Solomatov, M. Wysession, A. Hutko, E. Garnero, K. Hirose, R. Wentzcovich, and Q. Williams for comments on the manuscript.

References

Akber-Knutson, S., G. Steinle-Neumann, and P. D. Asimow (2005), The effect of Al on the sharpness of the $MgSiO_3$ perovskite to post-perovskite phase transition, *Geophys. Res. Lett.*, *32*, L14303, doi:10.1029/2005GL023192.

Hernlund, J. W., C. Thomas, and P. J. Tackley (2005), A doubling of the post-perovskite phase boundary and structure of the Earth's lowermost mantle, *Nature*, *434*, 882–886.

Hirose, K. (2006), Postperovskite phase transition and its geophysical implications, *Rev. Geophys.*, *44*, RG3001, doi:10.1029/2005RG000186.

Hutko, A. R., T. Lay, E. J. Garnero, and J. Revenaugh (2006), Seismic detection of folded, subducted lithosphere at the core-mantle boundary, *Nature*, *441*, 333–336.

Lay, T. and E. J. Garnero (2007), Reconciling the post-perovskite phase with seismological observations of lowermost mantle structure, in *Post-Perovskite*: *The Last Mantle Phase Change*, *Geophys. Monogr. Ser.*, vol. 174, edited by K. Hirose et al., pp. 129–153, AGU, Washington, D. C.

Lay, T., and D. V. Helmberger (1983), A lower mantle S-wave triplication and the shear velocity structure of D″, *Geophys. J. R. Astron. Soc.*, *75*, 799–837.

Lay, T., E. J. Garnero, and S. A. Russell (2004), Lateral variation of the D″ discontinuity beneath the Cocos Plate, *Geophys. Res. Lett.*, *31*, L15612, doi:10.1029/2004GL020300.

Mao, W. L., G. Shen, V. B. Prakapenka, Y. Meng, A. J. Campbell, D. L. Heinz, J. Shu, R. J. Hemley, and H. K. Mao (2004), Ferromagnesian post-perovskite silicates in the D″ layer of the Earth, *Proc. Natl. Acad. Sci.*, *101*, 15,867–15,869.

Murakami, M., K. Hirose, K. Kawamura, N. Sata, and Y. Ohishi (2004), Post-perovskite phase transition in $MgSiO_3$, *Science*, *304*, 855–858.

Ohta, K., K. Hirose, T. Lay, N. Sata, and Y. Ohishi (2008), Phase transitions in pyrolite and MORB at lowermost mantle conditions: Implications for a MORB-rich pile above the core-mantle boundary, *Earth Planet. Sci. Lett.*, in press.

Tateno, S., K. Hirose, N. Sata, and Y. Ohishi (2007), Solubility of FeO in $(Mg,Fe)SiO_3$ perovskite and the post-perovskite phase transition, *Phys. Earth Planet. Inter.*, *160*, 319–325.

Thomas, C., E. J. Garnero, and T. Lay (2004), High-resolution image of lowermost mantle structure under the Cocos Plate, *J. Geophys. Res.*, *109*, B08307, doi:10.1029/2004JB003013.

Tsuchiya, T., and J. Tsuchiya (2006), Effect of impurity on the elasticity of perovskite and postperovskite: Velocity contrast across the postperovskite transition in $(Mg,Fe,Al)(Si,Al)O_3$, *Geophys. Res. Lett.*, *33*, L12S04, doi:10.1029/2006GL025706.

Wysession, M. E., T. Lay, J. Revenaugh, Q. Williams, E. J. Garnero, R. Jeanloz, and L. H. Kellogg (1998), The D″ discontinuity and its implications, in *The Core-Mantle Boundary Region*, *Geodyn. Ser.*, vol. 28, edited by M. Gurnis et al., pp. 273–297, AGU, Washington, D. C.

T. Lay, Department of Earth and Planetary Sciences, University of California, Santa Cruz, Santa Cruz, CA 95064, USA. (thorne@pmc.ucsc.edu)